Biophysical Journal, Volume *120*

Supplemental information

Spatial control over near-critical-point operation ensures fidelity of Par-ABS-mediated DNA partition

Longhua Hu, Jérôme Rech, Jean-Yves Bouet, and Jian Liu

SUPPLEMENTAL INFORMATION

LH Hu, J Rech, JY Bouet, J Liu

SECTION I. MODEL PARAMETER TABLE

SECTION II. SUPPLEMENTAL FIGURES

SECTION III. SUPPLEMENTAL REFERENCE

SECTION I. MODEL PARAMETER TABLE

Table S1

Parameter	Physical meaning	Value range	Nominal chosen value	Reference
k_{nl}	Nucleoid elongation rate	6 – 18 nm/min	12 nm/min	Our exp
k_{syn}	ParA synthesis rate	0 – 100 /min	30 /min	Estimated from (1, 2) & our exp
k_{on}	Rate of ParA-ParB bond formation	10^3 – 10^4/sec	3300/sec	Estimated from (3)
k_{off}	Rate of ParA-ParB bond dissociation	~ 1.0/sec	1.0/sec	(4, 5)
k_a	Rate of cytosolic ParA·ATP binding to nucleoid	0.01–5.0/sec	3.0/sec	(3-7)
k_n	Rate of $ParA^D$ conversion to ParA·ATP	~ 0.1/sec	0.1/sec	(3)
$k_{d,T}$	Rate of ParA·ATP-nucleoid dissociation	~ 0.01/sec	0.01/sec	(4, 5)
$k_{d,D}$	Rate of $ParA^D$-nucleoid dissociation	~ 5.0/sec	5.0/sec	(4, 5)
D_p	Diffusion constant of PC	~ 10^3 -10^4 nm^2/sec	10^4 nm^2/sec	(8)
$D_{T,N}$	Diffusion constant of ParA·ATP along nucleoid	(1-5)×10^3 nm^2/sec	1250 nm^2/sec	(5, 9)
$D_{D,N}$	Diffusion constant of $ParA^D$ along nucleoid	(1-5)×10^3 nm^2/sec	1250 nm^2/sec	(5, 9)
$D_{T,C}$	Diffusion constant of cytosolic ParA·ATP	~ 10^5 nm^2/sec	10^5 nm^2/sec	(5, 9)
$D_{D,C}$	Diffusion constant of cytosolic $ParA^D$	10^3 nm^2/sec	10^3 nm^2/sec	(5, 9)
K_S	Spring constant of ParA-ParB bond	0.2 pN/nm	0.2 pN/nm	Estimated in (10, 11)
R	Radius of PC	100 nm	100 nm	(1, 12)
ρ_B	ParB density on PC	~0.013/nm^2	0.013/nm^2	(1)
L_e	Equilibrium ParA-ParB bond length	50 nm	50 nm	Estimated in (11, 13)
L_a	Maximal length for a newly formed bond	53 nm	53 nm	Estimated in (11, 13)
L_m	Maximal bond length extension	10 nm	10 nm	Estimated in (11, 13)
$k_{d,\ plasmid}$	Rate of PC-bound ParA·ATP dissociation	~ 5.0/sec	5.0/sec	

$k_{\text{a, plasmid}}$	Rate of cytosolic ParA·ATP-PC association	10 - 1000/sec	100.0/sec	
N_C^{PC}	Upper limit of PC-localized ParA number	100-1500	500	(4, 5)
k_a'	Rate of PC-bound ParA re-binding to nucleoid	$< k_a$	0.3/sec	(4, 5)

Note: The current model is built upon our established models (11, 13), in which we have done extensive parameter sensitivity test for most of the model parameters (*i.e.*, those in the Table S1 that are not in shaded box). These parameter sensitivity tests suggest that the essential features of the model – including those presented in Figs. 2 and 4 this paper – can be preserved in a broad range of model parameter space. The new ingredients in our current model pertain to the PC-localization of ParA, whose effects are characterized by the model parameters in shaded box in the Table S1. We have extended our parameter sensitivity tests to these parameters, the results of which are formulated as the model phase diagrams in Fig. 5C in the main text and Fig. S4 in the Section II (see below).

SECTION II. SUPPLEMENTAL FIGURES

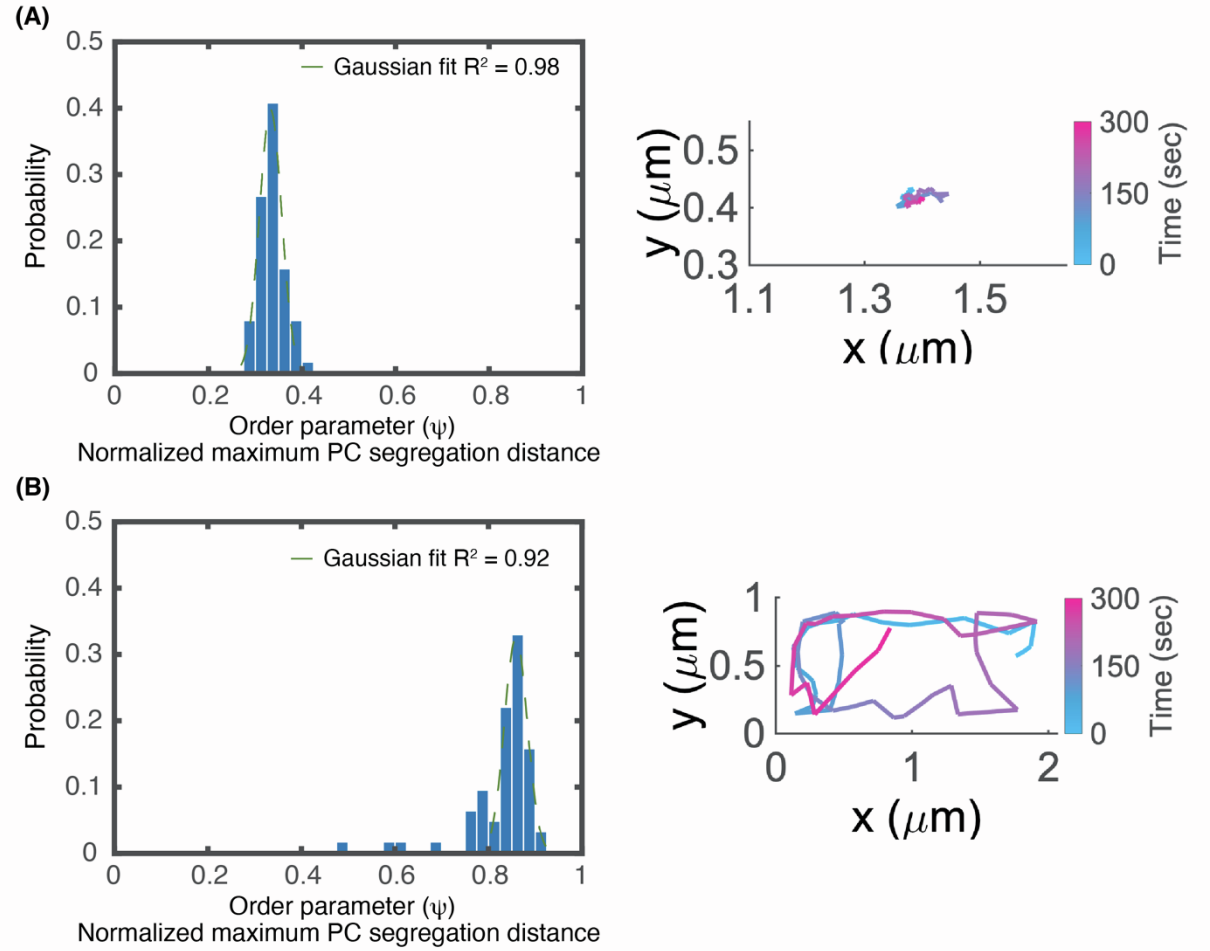

Fig. S1. Statistical distributions of order parameter, ψ (left) and representative simulation trajectories of PC movement (right) in the parameter regimes away from the critical point. (A) Near-static case (deep in the directed segregation regime). (B) Pole-to-pole oscillation. Note that, we calculated 1) the χ^2-value between the cumulative distribution function (CDF) of our data and Gaussian distribution and 2) the excess kurtosis values for (A) and (B). For the near-static case in (A), the χ^2-value and excess kurtosis value are 3.0 and -0.4, respectively. This suggests that the near-static case is closer to a Gaussian distribution than the case at the critical point in Figs. 2C and 2D, whose corresponding statistical measures are 6.6 and -1.0, respectively. In comparison, for the pole-to-pole oscillation in (B) the χ^2-value and excess kurtosis value are 21.0 and 8.0, respectively. This analysis result indicates that the excursion distribution in pole-to-pole oscillation is even more non-Gaussian than the case at the critical point. This is because, the excursion distribution of pole-to-pole oscillation has a long tail, which stems from the cases that the two PCs either have head-on collision and/or travel together, as shown in our previous work (13). Although the PCs move back and forth between the two poles for most of the time, these entanglements hinder the PC excursion and thus skew the distribution. As we previously suggested (13), because the two PCs are susceptible to traveling together if the partition machinery operates in the pole-to-pole oscillation regime, the partition fidelity (*i.e.*, the probability of having the two PCs in the two different cell halves) is predicted to be highly variable. This could explain the observation that only ~ 1% of *E. coli* displays pole-to-pole oscillation in low-copy plasmid partition, further

suggesting that the operating point of ParAB*S* system could be shaped by evolution to maximize the partition fidelity.

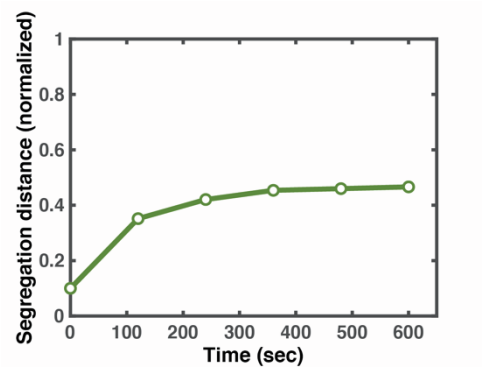

Fig. S2. PC segregation distance over time. Here, an example is provided to show that PC segregation distance (operating at the critical point in Fig. 2C) has already reached the steady state at t =10 minutes. As such, our analysis is not expected to change much for a longer simulation. Additionally, we used 10-min of simulation run to faithfully compare with our experimental data, which is also 10-min in duration.

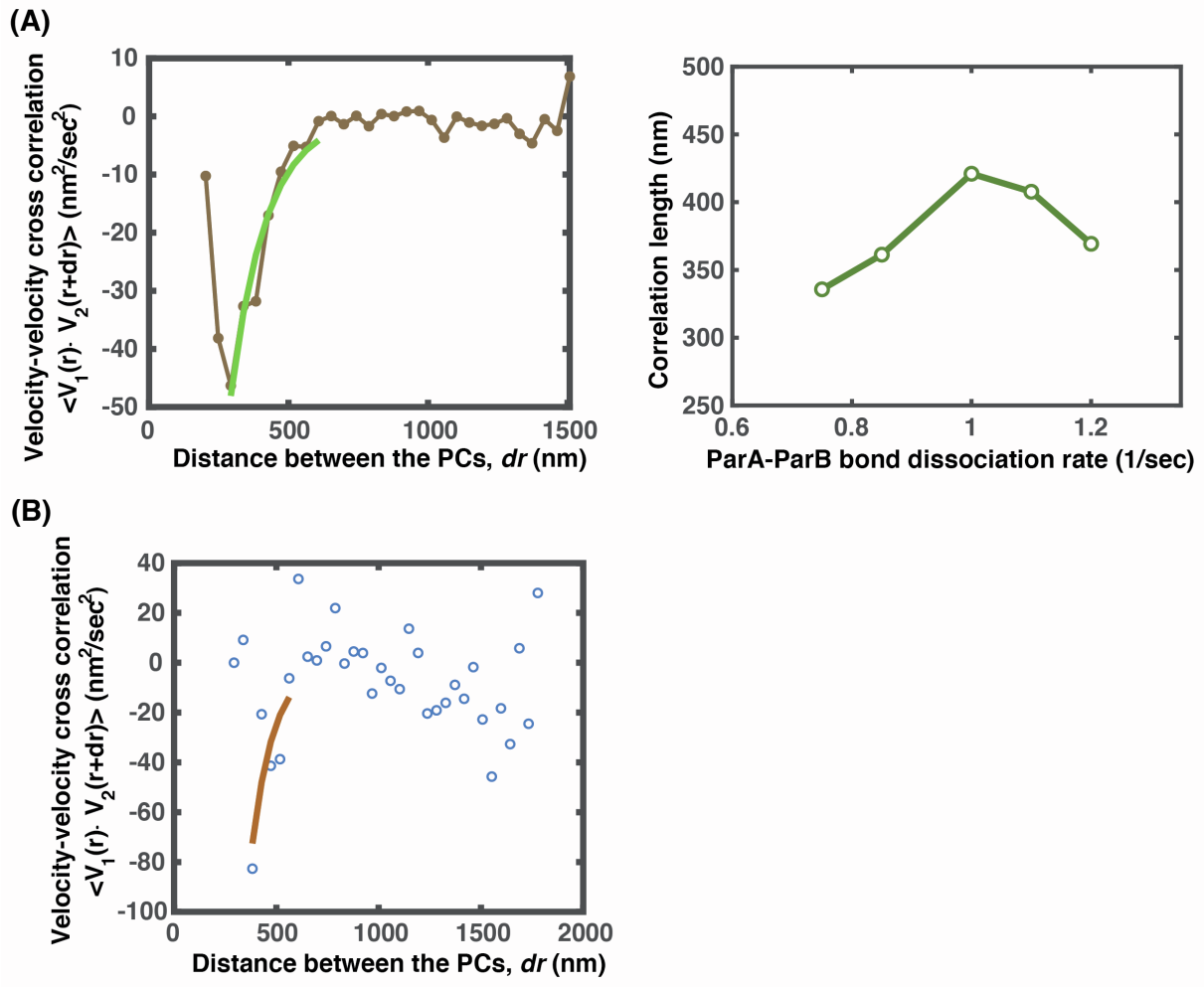

Fig. S3. Correlation function of PC movements. (A) Model result. Left: Cross-correlation function of PC movements vs. distance between the PCs for the case at the critical point. Right: Plot of correlation length vs. k_{off}. It shows that the correlation length peaks (~ 400 nm) at the critical point. (B) Experimental data of cross-correlation function of PC movement vs. distance. The correlation length of PC movement is determined to be ~ 500 nm. For (A) and (B), the velocity cross correlation function is calculated from $\langle \vec{V}_1(r) \cdot \vec{V}_2(r+dr) \rangle$, where the subscripts 1 and 2 denotes the pair of PCs in a cell, separated by the distance between the PCs, *dr*, and the <...> denotes the ensemble average. Additionally, the ensemble average is over 64 and 60 pairs of PCs for the model result (A) and for the experiment (B), respectively. The correlation function displays a peak of negative value at some distances, indicating that the movements of PCs are correlated when they undergo directed segregation. To compute the correlation length, the decreasing part of the peak is fit with the exponential function a·exp(-dr/L_C) (*i.e.*, the green curve in (A) and the brown curve in (B)), which yields the characteristic length L_C. The peak occurs at the distance L_P due to the excluded volume effect between the PCs. The correlation length is $L_C + L_P$, the sum of the characteristic length, L_C and the peak position, L_P.

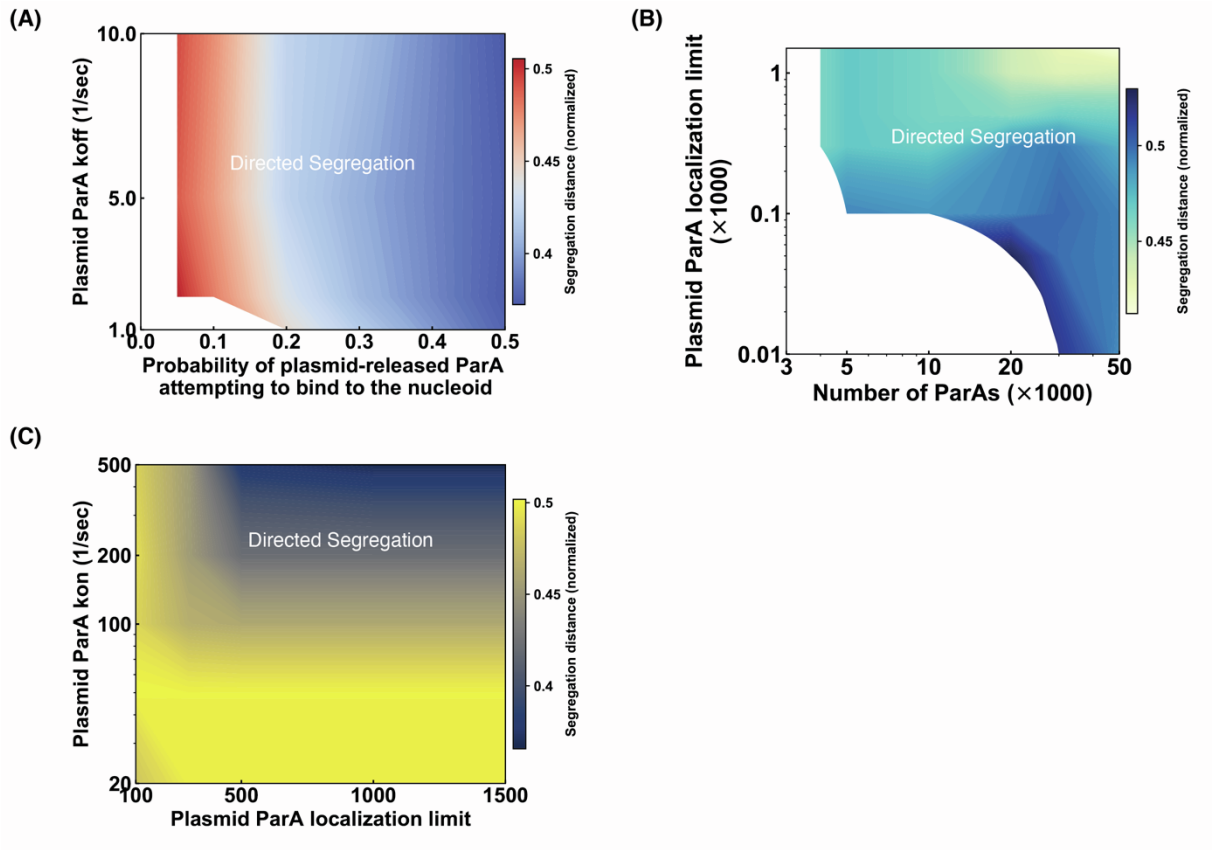

Fig. S4. Model phase diagram studies of PC-ParA localization effects on PC partitioning. (A) ParA turnover rate from PC vs. percentage of PC-released ParA that binds to nucleoid. (B) Saturation level of PC-localized ParA vs. total ParA number. (C) ParA binding rate onto PC vs. Saturation level of PC-localized ParA. For (A-C): We varied the two parameters in the respective phase diagrams, while keeping the rest of the model parameters fixed in accordance with the nominal chosen values in the Table S1. For each point in the phase diagram, we ran stochastic simulations for ≥ 36 trajectories of 10 min-dynamical evolution of the system, starting from the same initial condition and parameter set. The segregation distance reports the average value of ≥ 36 trajectories at the end of the simulation.

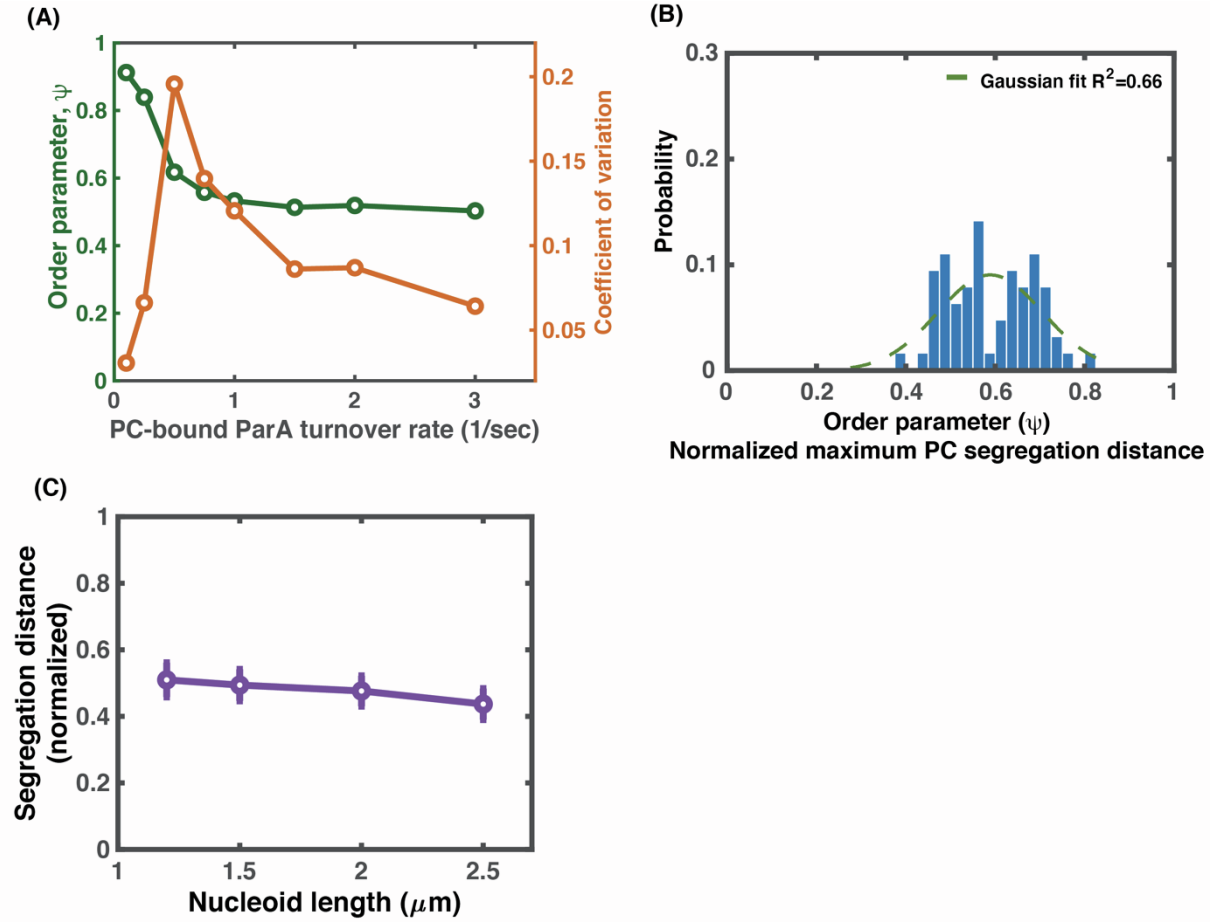

Fig. S5. Full model with PC-localization of ParA preserves all the essence of near-tipping-point partition as that in Fig. 2. (A) Order parameter and its variation as functions of PC-bound ParA turnover rate. (B) Statistical distribution of the order parameter, ψ, near the critical point. (C) Segregation distance adapts to half of the nucleoid lengths near the tipping point in the parameter space. The parameter set ($k_{a,\,plasmid}$, $k_{off,\,plasmid}$) used here is the same as that in Fig. 5B.

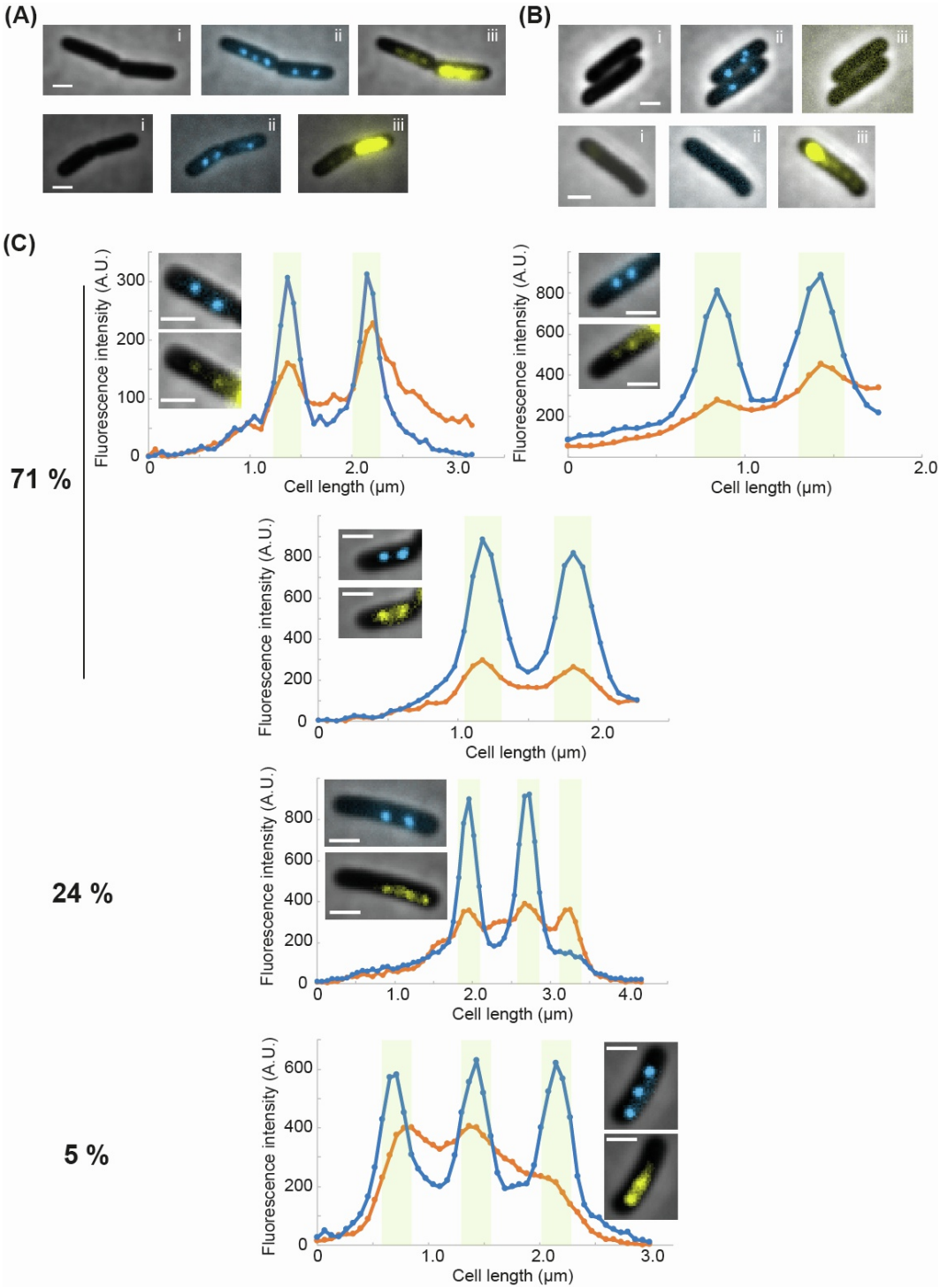

Fig. S6. Co-localization of $ParA_F$ foci and partition complexes. (A) Two typical examples of asymmetric inheritance of $ParA_F$ upon cell division. Due to the oscillatory behavior of $ParA_F$, most often one cell inherits most of $ParA_F$ while the other a much smaller amount. Dividing cells are observed in phase contrast (i) and in fluorescence microcopy to observe $ParB_F$-mTq2 (ii, blue channel) or $ParA_F$-mVenus (iii, yellow channel) in overlay with phase contrast. Cells were grown at 30°C in MGlyC. (B) Fluorescence signals are specifically detected without spreading in other channels. Strains carrying mini-F plasmids expressing either only $ParB_F$-mTurquoise (pJYB240; top) or only $ParA_F$-mVenus (pJYB243, bottom) are grown and imaged as in (A). No leaky signal from mTurquoise2 or mVenus is observed in the yellow (iii) or blue (ii) channels, respectively. (C) Line scan analyses of fluorescence intensity

along cell length. Blue and orange lines correspond to the blue ($ParB_F$-mTq2) and yellow ($ParA_F$-mVenus) channels, respectively. The corresponding cell images is displayed in the graph as in (A). Over 58 cells, 41 (71%) displayed the same number of ParA and ParB foci, 14 (24%) displayed more ParA than ParB foci, and 3 (5%) displayed more ParB than ParA foci. The light green area corresponds to the limit of resolution of the microscope (i.e. 4 pixels (262 nm) around the PC peaks). Scale bar: 1 μm in all images.

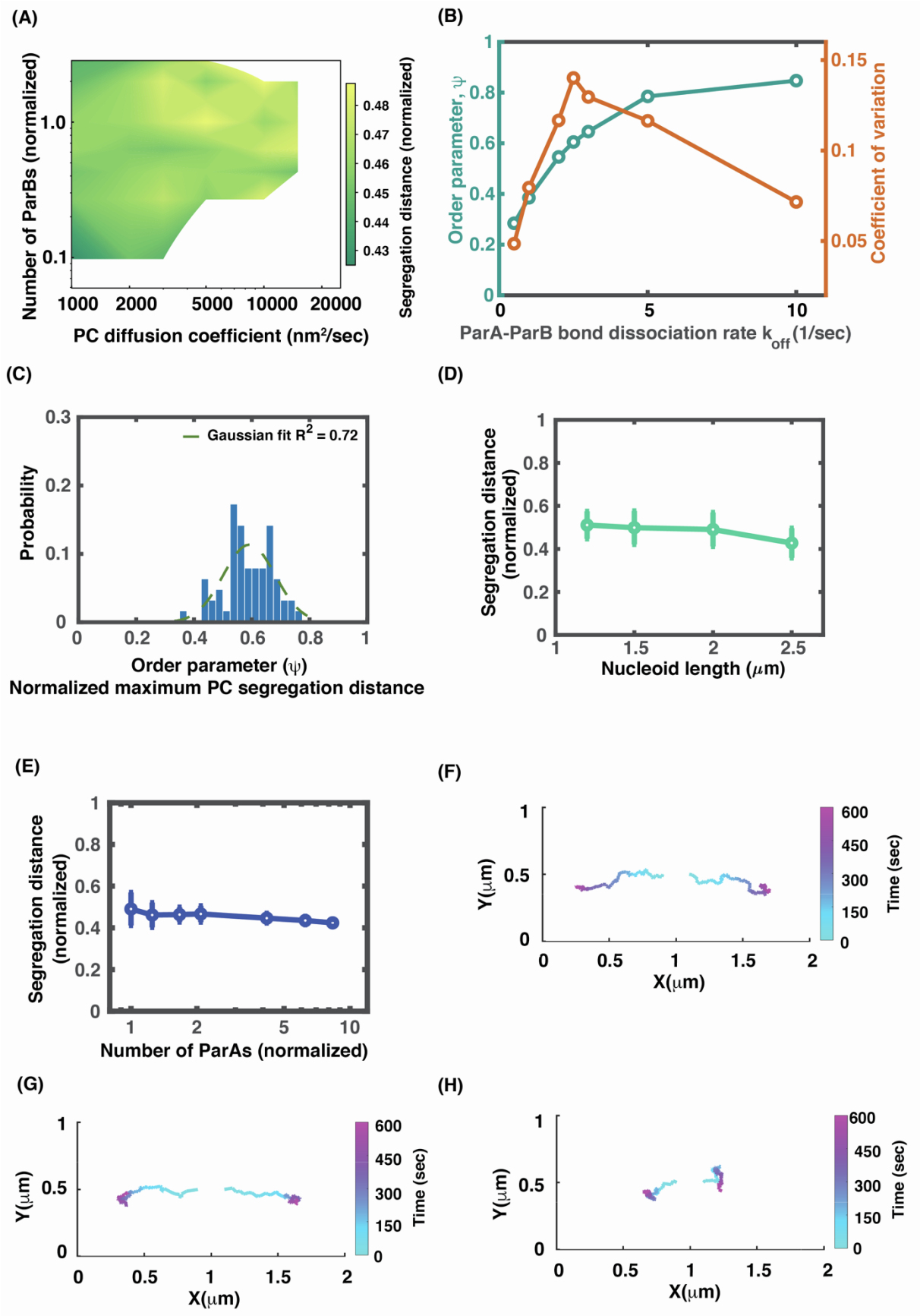

Fig. S7. Model exploration of potential impacts of PC moving inside nucleoid on PC partition. The explored effects include the combination of a slower PC diffusion and variation

in the number of PC-bound ParB available for ParA binding (A-E), and non-uniform nucleoid DNA distribution (F-H). Here, all the model calculations are performed with the full model that depicts the PC-localization of ParA. (A) Computed phase diagram of the dependence of PC segregation on PC diffusion coefficients and the number of PC-bound ParBs that is available for ParA binding. (B) Characteristics of the near-tipping-point operation. (C) Statistical distribution of order parameter, ψ, near the critical point. (D) The segregation distance adapts to half-lengths of the nucleoid near the tipping point. The parameter set of ($k_{a,\ plasmid}$, $k_{off,\ plasmid}$) used here is the same as that in Fig. 5B. (E) Segregation distance adaptation buffers against the variations in the ParA level. For (B-E), the PC diffusion coefficient is chosen to be 2000 nm^2/sec, 5 times slower than that in Fig. 5. (F-H) Non-uniform nucleoid DNA density directs PC movement. PCs move on the nucleoid substrate surface with non-uniform DNA density along the x-direction. Three cases were simulated: (F) the density of nucleoid DNA increases from the center to the poles; (G) the density of nucleoid DNA increases from the center to the quarter positions; and (H) the density of nucleoid DNA decreases from the center to the poles. A typical simulated trajectory is shown for each case, and normalized segregation distance averaged over 36 independent trajectories are (F) 0.69, (G) 0.63 and (H) 0.27, respectively.

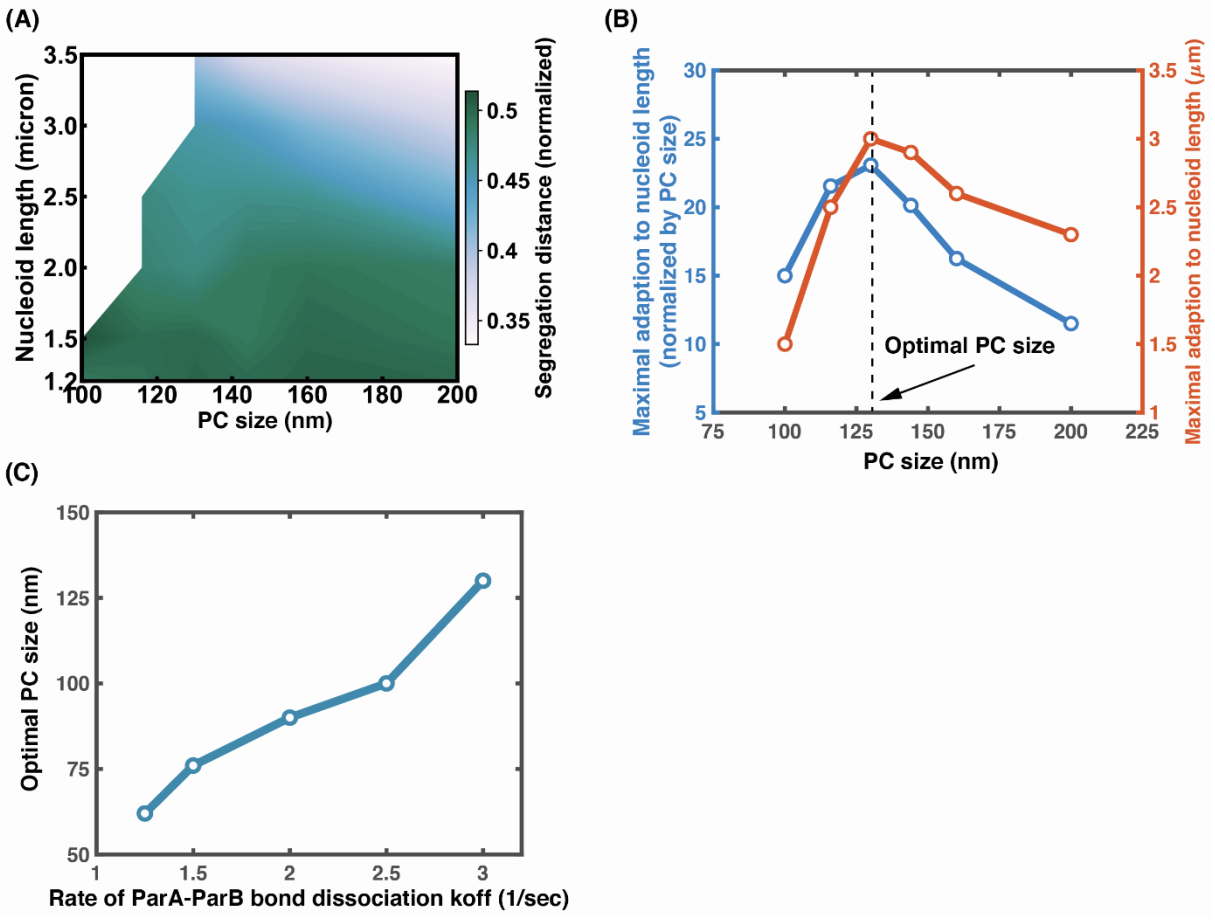

Fig. S8. Spatial control over near tipping-point operation defines an optimal PC size for maximal partition adaptation of nucleoid length. (A) Nucleoid length vs. PC size. The color bar represents the relative PC segregation distance, i.e., the PC segregation distance divided by the nucleoid length at 10-min time mark. (B) Maximal nucleoid length of partition adaptation vs. PC size. We used the relative PC segregation distance of 0.45 as the threshold, above which we termed the PC partition as being faithful. As such, the maximal nucleoid length at a given PC size is defined as the longest nucleoid length for faithful partition of the corresponding PC. While keeping all other model parameters fixed, we varied the PC size along with 1) the corresponding maximum number of PC-localized ParA (i.e., proportional to the PC surface area) and 2) diffusion coefficient of PC (*i.e.*, proportional to the inverse of PC diameter). (C) ParA-ParB bond dissociation rate vs. optimal PC size. To obtain this curve, we varied k_{off} near the transition line between "pole-to-pole oscillation" and "directed segregation" in the phase diagram of Fig. 2A, and then repeated the calculation in (B) to determine the corresponding optimal PC size.

SECTION III. SUPPLEMENTAL REFERENCE

1. Sanchez, A., Diego I. Cattoni, J.-C. Walter, J. Rech, A. Parmeggiani, M. Nollmann, and J.-Y. Bouet. 2015. Stochastic Self-Assembly of ParB Proteins Builds the Bacterial DNA Segregation Apparatus. Cell Systems 1(2):163-173.
2. Yates, P., D. Lane, and D. P. Biek. 1999. The F plasmid centromere, sopC, is required for full repression of the sopAB operon. Journal of Molecular Biology 290(3):627-638.
3. Vecchiarelli, A. G., Y.-W. Han, X. Tan, M. Mizuuchi, R. Ghirlando, C. Biertümpfel, B. E. Funnell, and K. Mizuuchi. 2010. ATP control of dynamic P1 ParA–DNA interactions: a key role for the nucleoid in plasmid partition. Molecular Microbiology 78(1):78-91.
4. Hwang, L. C., A. G. Vecchiarelli, Y. W. Han, M. Mizuuchi, Y. Harada, B. E. Funnell, and K. Mizuuchi. 2013. ParA‐mediated plasmid partition driven by protein pattern self‐organization. The EMBO Journal 32(9):1238-1249.
5. Vecchiarelli, A. G., L. C. Hwang, and K. Mizuuchi. 2013. Cell-free study of F plasmid partition provides evidence for cargo transport by a diffusion-ratchet mechanism. Proceedings of the National Academy of Sciences 110(15):E1390-E1397.
6. Castaing, J.-P., J.-Y. Bouet, and D. Lane. 2008. F plasmid partition depends on interaction of SopA with non-specific DNA. Molecular Microbiology 70(4):1000-1011.
7. Hatano, T., and H. Niki. 2010. Partitioning of P1 plasmids by gradual distribution of the ATPase ParA. Molecular Microbiology 78(5):1182-1198.
8. Vecchiarelli, A. G., K. C. Neuman, and K. Mizuuchi. 2014. A propagating ATPase gradient drives transport of surface-confined cellular cargo. Proceedings of the National Academy of Sciences 111(13):4880-4885.
9. Surovtsev, Ivan V., Hoong C. Lim, and C. Jacobs-Wagner. 2016. The Slow Mobility of the ParA Partitioning Protein Underlies Its Steady-State Patterning in Caulobacter. Biophysical Journal 110(12):2790-2799.
10. Bustamante, C., S. B. Smith, J. Liphardt, and D. Smith. 2000. Single-molecule studies of DNA mechanics. Current Opinion in Structural Biology 10(3):279-285.
11. Hu, L., A. G. Vecchiarelli, K. Mizuuchi, K. C. Neuman, and J. Liu. 2015. Directed and persistent movement arises from mechanochemistry of the ParA/ParB system. Proceedings of the National Academy of Sciences 112(51):E7055-E7064.
12. Lim, H. C., I. V. Surovtsev, B. G. Beltran, F. Huang, J. Bewersdorf, and C. Jacobs-Wagner. 2014. Evidence for a DNA-relay mechanism in ParABS-mediated chromosome segregation. eLife 3:e02758.
13. Hu, L., A. G. Vecchiarelli, K. Mizuuchi, K. C. Neuman, and J. Liu. 2017. Brownian Ratchet Mechanism for Faithful Segregation of Low-Copy-Number Plasmids. Biophysical Journal 112(7):1489-1502.